Journal of Catalysis 267 (2009) 30–39

Contents lists available at ScienceDirect

Journal of Catalysis

journal homepage: www.elsevier.com/locate/jcat

Enhancement of biphenyl hydrogenation over gold catalysts supported on Fe-, Ce- and Ti-modified mesoporous silica (HMS)

Pedro Castaño [a], T.A. Zepeda [b], B. Pawelec [c], Michiel Makkee [a], J.L.G. Fierro [c,*]

[a] Delft University of Technology, Catalysis Engineering, Julianalaan 136, NL2628 BL Delft, Netherlands
[b] Centro de Nanociencias y Nanotecnología – UNAM, Km. 107 Carretera Tijuana-Ensenada, CP. 22800, Ensenada, B.C., Mexico
[c] Instituto de Catálisis y Petroleoquímica, CSIC, c/Marie Curie 2, Cantoblanco, 28049 Madrid, Spain

ARTICLE INFO

Article history:
Received 29 May 2009
Revised 16 July 2009
Accepted 17 July 2009
Available online 19 August 2009

Keywords:
Poly-aromatic
Liquid hydrogenation
Mesoporous silica
Au catalysts
Au–Ce catalyst

ABSTRACT

Mesoporous metallosilicates (HMS–M; M = Ce, Fe, Ti) were used as supports for the preparation of Au catalysts, and were tested in the liquid-phase hydrogenation of biphenyl at 5 MPa and 488 K. Irrespective of the support, uniformly dispersed Au nanoparticles in range 3.2–6.5 nm were obtained. The highest turn over frequency (TOF), expressed per surface Au atom, was achieved on the Au/HMS–Fe, furthermore this catalyst gave the highest selectivity to the most saturated compound (bicyclohexyl with the highest cetane number) by means of enhancing the second aromatic-ring hydrogenation. From the catalyst activity-structure correlation, the highest activity of the Au/HMS–Fe catalyst is linked with: (i) the higher ratio of positively charged metallic gold $Au^{\delta+}$/Si (XPS), and (ii) the higher stability of Au nanoparticles (HRTEM). A linear correlation between the activity (per gram of metal) of the catalysts and their ratio $Au^{\delta+}$/Si is observed; however, Au/HMS–Ce catalyst displays a different behaviour in terms of activity per gram of metal exposed caused by the fact that ceria is not incorporated in the framework.

1. Introduction

In the present decade, the environmental challenges for producing sufficient and better quality diesel fuel are accentuated to meet the demand and the legislations. In particular, the polycyclic aromatic hydrocarbons (PAHs) have to be reduced because they are hazardous for the humans and the environment [1,2]. The reduction of aromatics in diesel via hydrotreatment has been the basic route for reaching the actual standards in terms of cetane number (up to values of 51) and density(<845 kg m^{-3}). Traditional NiMo(P)/γ-Al_2O_3 catalysts could not fulfil the required specifications so the challenge was to design stable hydroprocessing catalysts based on noble metals (with higher activity) [3].

It is anticipated that the hydrogenation (HYD) rates on Au-supported catalysts are slower in comparison to that on Pt- or Pd-supported ones. This is because Au has a limited capacity to dissociate H_2 molecules due to the completely filled electronic *d*-band [4]. Several authors [5,6], however, demonstrated that nano-sized Au prepared by deposition–precipitation (DP) exhibits improved activity in the oxidation of CO at low temperatures. Recently, Au catalysts have shown high activity and selectivity for a number of reactions involving H_2 [7,8], e.g. aromatic hydrogenation in the presence of dibenzothiophene [9–11] and thiophene–dibenzothiophene hydrodesulphurization [12,13]. The nature of the active phase of Au catalyst is still controversial: the metallic Au^0 [14] or the cationic Au^{3+} [15,16]. This could be due to the fact that it is difficult to detect Au^{3+} and positively charged metallic gold ($Au^{\delta+}$) with some extended techniques as XPS [17]. A novel approach is to embed Au^{3+} species in metal-organic frameworks [18].

Concerning the support, our previous study showed that Au supported on SiO_2 catalyst exhibited larger activity than the γ-Al_2O_3-supported counterpart in the naphthalene hydrogenation [9]. Those results prompt us to prepare nano-sized Au catalysts supported on hexagonal mesoporous silica (HMS). In comparison with SiO_2, the HMS shows much weaker metal-support interaction, but it offers a larger surface area and wormhole mesostructure for diffusing reactants and products. Co(Ni)Mo/HMS catalysts exhibited an excellent catalytic ability for hydrotreating reactions [19–22]. The one-pot synthesis of HMS offers further opportunities for the incorporation of transition metals into the silica framework. The stabilization occurs by substitution of Si^{4+} by Ti^{4+} and Al^{3+} [21,23]. On one hand, it has been demonstrated that HMS–Fe support (i) is more hydrothermally stable than pure HMS [24], (ii) is highly efficient for the hydroxylation of phenol [25], and (iii) exhibits high activity for the alkylation of benzene with benzyl chloride [26]. On the other hand, Au/Fe_xO_y catalysts were found to be effective in the liquid-phase hydrogenation of α, β-unsaturated ketones [27]. Similar to Fe, one might expect that the incorporation of Ce^{4+} ions into the framework of HMS network might impact simultaneously on

* Corresponding author. Fax: +31 0 1527 85006.
E-mail address: jlgfierro@icp.csic.es (J.L.G. Fierro).

0021-9517/$ - see front matter © 2009 Elsevier Inc. All rights reserved.
doi:10.1016/j.jcat.2009.07.011

Nomenclature

Aw_{Au}	atomic weight of gold in g/mol
C	concentration in g/L or mol/L
C^0	initial concentration in g/L or mol/L
D_{eff}	effective diffusivity
Dp	particle diameter in nm or m
k	pseudo-first kinetic constant in $g_{BPH}/g_{cat} \cdot h$
Mw	molecular weight in g/mol
N_A	Avogadro number
$-r_{max}$	maximum hydrogenation rate
t	time in h or s
S	surface density of Au in at_{Au}/cm^2
V	volume of reactor in L
Wc	weight of catalyst in g_{cat}
X	conversion of biphenyl, Eq. (1)
Z	conversion of aromatics, Eq. (2)

Abbreviations and subscripts

BPH, CHB, BCH	biphenyl, cyclohexylbenzyl, bicyclohexyl
DP	deposition–precipitation method
HYD	hydrogenation
PAH	polycyclic aromatic hydrocarbons
QTOF	turn over frequency in $mol_{BPH}/mol_{Au\text{-}total} \cdot s$, Eq. (5)
TOF	turn over frequency in $mol_{BPH}/mol_{Au\text{-}exposed} \cdot s$, Eq. (4)
WHSV	weigh hourly space velocity in $g/g_{cat} \cdot h$

Greek symbols

v	weight proportion of Au in the catalyst in g_{Au}/g_{cat}
ρ	density in g/cm^3
Φ_{WP}	Weisz–Prater module, Eq. (6)
τ	batch space time in $g_{cat} \cdot h/g_{BPH}$, Eq. (3)

the redox and acidic properties of the support [28], enhancing the hydrogenation reaction [29].

Within this background information, the present study investigated the properties and hydrogenation performance of Au supported on HMS modified with Ce, Fe and Ti. Biphenyl HYD was selected as the test reaction because it is a by-product of dibenzothiophene hydrodesulphurization, and jointly with naphthalenes forms the majority of aromatics in diesel. The structural and surface characterization of the samples was performed by means of different techniques (N_2 adsorption–desorption isotherms, TPD-NH_3, HRTEM, X-ray photoelectron spectroscopy (XPS) and TPO/TGA techniques).

2. Experimental

2.1. Support/catalyst preparation

Hexagonal mesoporous silica (HMS) was synthesized by neutral S^0I^0 templating route, which is based on hydrogen bonding and self-assembly between neutral primary amine surfactants (S^0) and a neutral inorganic precursor (I^0) [30]. Tetraethylorthosilicate (TEOS, 98% Aldrich) was used as a neutral silica precursor, whereas dodecylamine (DDA, Aldrich 99%) and mesitylene (C_9H_{12}, Aldrich 98%) were used as a neutral structure director and a swelling organic agent, respectively, as firstly proposed by Kresge et al. [31]. Furthermore, the excess of HCl was employed and the synthesis was performed at 335 K. The reaction products were filtered, washed with distilled water and dried at room temperature for 24 h, followed by drying at 378 K for 2 h. Subsequently, the sample was calcined in air at 823 K for 3.5 h with a heating rate of 2.5 K/min. The metallosilicates (HMS–M; M = Ce, Fe, Ti) were prepared by dissolving the appropriate amounts of cerium nitrate hexahydrate (Aldrich 99%), iron(III) nitrate nonahydrate (Aldrich 98%) or tetrabutyl orthotitanate (Aldrich 98%) in TEOS in order to obtain samples with a Si/M (M = Ce, Fe, Ti) atomic ratio of 40. The drying, washing and calcination steps were the same as described above for the HMS material.

The supported Au/HMS, Au/HMS–Ce, Au/HMS–Fe and Au/HMS–Ti catalysts were prepared by deposition–precipitation method using the $HAuCl_4$ as Au precursor. A solution of chloroauric acid in water was slowly added to a stirred suspension of 2 g of support in water. The pH of the solution was kept at 9.0 with aqueous ammonia (Merck, 25%), and the solution was aged for 30 min at room temperature. The chlorine ions were removed by washing the sample with warm distilled water followed by drying in air overnight at 323 K. Finally, calcination was performed at 573 K for 3 h.

2.2. Characterization techniques

2.2.1. Chemical analysis

Atomic Emission Spectroscopy (ICP-AES) was used for the determination of the Au loading in the calcined catalysts by means of a Perkin Elmer Optima 3300DV spectrometer. The solid samples were digested (in a mixture of HF, HCl and HNO_3) in a microwave oven for 2 h. Then, aliquots of solution were diluted to 50 mL using deionized water (18.2 mΩ quality).

2.2.2. N_2 adsorption–desorption isotherms

N_2 adsorption–desorption isotherms (at 77 K) were used for the determination of surface area (BET method), pore volume and pore size distribution (BJH method) of the pure supports and calcined catalysts, degassed at 543 K in vacuum for 5 h, using a Micromeritics TriStar 3000 apparatus.

2.2.3. Temperature-programmed desorption technique

Temperature-programmed desorption of ammonia (TPD-NH_3) was employed for the determination of the number of acid sites of the supports, using a Micromeritics 2900 equipment provided with TCD detector. After loading, the sample of 50 mg was pretreated in a He (Air Liquide, 99.996%) stream at 573 K for 1 h. Following this, the sample was cooled to 473 K and ammonia-saturated in a stream of 5% NH_3/He (Air Liquide) flow (50 mL/min) for 1 h. Then, after catalyst equilibration in a He flow at 400 K for 0.5 h the ammonia was desorbed using a heating rate of 10 K/min to 1350 K. The amount of desorbed ammonia was followed by thermal conductivity detector (TCD).

2.2.4. X-ray diffraction (XRD)

The catalysts were characterized by powder X-ray diffractometry according to the step-scanning procedure (step size 0.02°; 0.5 s) with a computerized Seifert 3000 diffractometer, using Ni-filtered CuKα (λ = 0.154 nm) radiation and a PW 2200 Bragg–Brentano $\theta/2\theta$ goniometer equipped with a bent graphite monochromator and an automatic slit. The assignment of the various crystalline phases was based on the JPDS powder diffraction file cards. The metal particle sizes were calculated from the line broadening of the most intense peak using the Debye–Scherrer equation.

2.2.5. UV–vis spectroscopy

The electronic spectra of the finely ground pure supports and calcined Au catalysts were recorded in the range of 200–900 nm at room temperature using a Varian Cary 5000 UV–vis spectrophotometer equipped with an integration sphere.

2.2.6. HRTEM measurements

High resolution transmission electron microscopy (HRTEM) studies of the spent catalysts were carried out using a JEM 2100F microscope operating with a 200 kV accelerating voltage and fitted with an INCA X-sight (Oxford Instruments) energy dispersive X-ray microanalysis (EDX) system to verify semi-quantitative composition of supported phases. Au nanoparticles were differentiated in all cases except for the Au/HMS–Ce catalyst where CeO_2 clusters show similar contrast as Au ones. In this case, the round morphology of Au nanoparticles and the difference in the distance between crystal planes (0.326 nm for CeO_2 [1 1 1] and 0.235 nm for Au^0 [1 1 1]) guided us to distinguish between the two metals.

2.2.7. X-ray photoelectron spectroscopy (XPS)

X-ray photoelectron spectroscopy (XPS) of the fresh reduced and spent catalysts was carried out on a VG Escalab 200 R electron spectrometer equipped with a hemispherical electron analyzer, using a Mg Kα ($h\nu$ = 1253.6 eV, 1 eV = 1.603×10^{-19} J) X-ray source.

2.2.8. Thermogravimetric analysis (TGA)

The quantity of coke deposited on the spent catalysts was determined by temperature-programmed oxidation (TPO) by thermogravimetry (TGA/SDTA851 Mettler Toledo), measuring the weight lost in the spent catalysts during oxidation. Each sample (ca. 30 mg) was previously heated in order to homogenize coke and remove the volatile compounds up to 773 K for 1 h in N_2 (10 K/min; 200 mL/min). Once the sample was cooled to 303 K (5 K/min) burning of coke was carried out by raising sample temperature to a final temperature of 1173 K at a rate of 10 K/min in a 20% O_2/N_2 gas mixture (50 mL/min). The data used correspond to temperatures up to 823 K since the catalysts had been previously calcined at this temperature and the HMS support could decompose. The amount of coke (+ reactant/products mixture in the pores of catalyst) present in the spent catalyst was calculated by the difference between initial weight and final weight of the catalyst sample, with the initial weight taken as the mass of the sample after pre-treatment at 773 K under N_2 at 1 h.

2.3. Catalytic activity measurements

The catalyst performance was measured in the liquid-phase hydrogenation of biphenyl in a slurry-type reactor: 0.3 L batch stirred reactor, Medimex Inc. The reaction procedure consisted in loading the catalyst (ca. 0.3 g) in the reactor and treating it *in-situ* under a flow of hydrogen of 80 mL/min, atmospheric pressure and 523 K for 2 h. Then the liquid mixture was loaded. The liquid mixture consisted in a solution (0.15 L) of *n*-tetradecane (Acros Organics, 99%), 10 g/L of *n*-hexadecane (Merck, 99%) as a reference compound and 10–12 g/L of biphenyl (Acros Organics, 98%) as a reactant. Traces of sulphur compounds were detected in the liquid mixture and, therefore, it was treated prior in an adsorbing bed (extrudates of Ni–NiO/Al_2O_3, atmospheric pressure, WHSV = 1 g/$g_{cat} \cdot$ h and 423 K) for decoupling the influence of poisoning on the kinetics. By the adsorption treatment the concentration of sulphur in the feedstock was reduced from 0.2–0.6 ppm to 0.01–0.02 ppm according to the results obtained with an internal standard solution of thiophene in a HP-4890 Series II gas-chromatograph, equipped with a Sulphur Chemiluminescence Detector (SCD). The reaction conditions were: pressure of 5 MPa, temperature of 488 K and stirring rate of 1200 rpm. Under these tailored conditions, the concentration of hydrogen is 56.5 g/L [32,33]. The analysis of un-reacted compounds and products was carried out in a ChromPack CP9001 gas chromatograph equipped with a 50 m HP-1 column and a Flame Ionization Detector (FID).

Biphenyl (BPH) is hydrogenated in series to form cyclohexylbenzyl (CHB) and subsequently bicyclohexyl (BCH). In order to account for these sequenced hydrogenations in the kinetics two different conversions have been defined:

$$X = \frac{C^0_{BPH} - C_{CHB} - C_{BCH}}{C^0_{BPH}} \tag{1}$$

$$Z = \frac{C^0_{BPH} - 1/2C_{CHB} - C_{BCH}}{C^0_{BPH}} \tag{2}$$

where C^0_{BPH} is the initial concentration of biphenyl, whereas C_{CHB} and C_{BCH} are the concentrations of cyclohexylbenzene and bicyclohexyl, respectively. X characterizes the hydrogenation of biphenyl, whereas Z characterizes the total aromatic hydrogenation in this reaction in series, giving values of the conversion over the entire range of operation.

The batch space time (τ) had been defined to compare the kinetic runs:

$$\tau = \left(\frac{Wc}{V \cdot C^0_{BPH}}\right) t \tag{3}$$

where V is the volume of reactive solution in the reactor (typically 0.15 L) and Wc is the weight of the catalyst.

The activity of the catalyst was determined on the basis of pseudo-first order kinetic linearization ($-\mathrm{Ln}(1 - X) = k \cdot \tau$), which is a much extended approach for this liquid-phase hydrogenation [34]. The Turn Over Frequency (TOF) is the optimal method to compare activity since it accounts for the number of accessible metallic sites for hydrogenation. TOF had been calculated using the following expression based on the assumption of cube-shaped particles whose five of six faces were accessible:

$$TOF = \frac{kN_A Dp_{Au} \rho_{Au}}{5 \upsilon_{Au} Mw_{BPH} S} \tag{4}$$

where N_A was the number of Avogadro, Dp_{Au} is the diameter of Au particles calculated from HRTEM results, ρ_{Au} is the density (19.3 g_{Au}/cm^3), υ_{Au} is the Au weight proportion in the catalyst measured by ICP, Mw_{BPH} is the molecular weight of BPH and S is the surface density (1.17×10^{15} at_{Au}/cm^2). Note that k has units inversed to τ ($g_{BPH}/g_{cat} \cdot h$). When the amount of accessible metallic sites cannot be precisely calculated, then it is optimal to measure activity in terms of total metallic sites (in $mol_{BPH}/mol_{Au} \cdot h$).:

$$QTOF = \frac{kAw_{Au}}{\upsilon_{Au} Mw_{BPH}} \tag{5}$$

where Aw_{Au} is the atomic weight of gold. The absence of external mass transfer limitations was assessed by selecting the optimal stirring rate and catalyst particle size combination in order to attain intrinsic kinetics with the more active commercial catalyst (per g_{cat}) based on Pt–Pt [35]. The absence of internal mass transfer limitation was verified by calculating the Weisz–Prater module (Φ_{WP}) for a first-order kinetic reaction:

$$\Phi_{WP} = \frac{(-r_{\max}) Dp^2}{D_{eff} C_{BPH}} \tag{6}$$

where $(-r_{max})$ is the maximum hydrogenation rate and D_{eff} is the effective diffusivity, derived from Wilke–Chang equation multiplied by the porosity over the tortuosity. Moreover, the hydrogenation runs were performed at conversions not higher than 25%, where

the influence of the internal mass transfer limitation can be neglected.

3. Results

3.1. Characterization of the fresh catalysts

3.1.1. Chemical, textural and acidic properties

Some physico-chemical properties of the calcined catalysts are summarized in Table 1. Chemical analysis revealed that Au content of Au/HMS–M (M = Ce, Fe, Ti) catalysts is a little larger than that of the Au/HMS sample (3.02–3.44 vs. 2.24 wt.%), considering the fact that the nominal content in all catalyst is 3.5 wt.%, we have to indicate that the efficiency of the Au-loading method increases after HMS modification with Ce, Fe or Ti. Furthermore, the results presented in Table 1 show that the efficiency of the Au-loading method increases with the Ce, Fe or Ti concentration, particularly for the Au/HMS–Ce catalyst. The textural properties of the calcined catalysts were evaluated from the nitrogen adsorption–desorption isotherms at 77 K (not shown here). According to the IUPAC classification, all supports show the N_2 isotherms of type IV and H1 hysteresis loops, which indicate the presence of textural meso-pores and uniform cylindrical pores. Au/HMS and Au/HMS–Ti catalysts show two capillary condensation steps: the first one at $P/P^0 \approx 0.40$ indicates the presence of framework meso-porosity, whereas the second one at $P/P^0 \approx 0.85$ is due to textural inter-particle meso-porosity or macro-porosity. Moreover, both Au/HMS–Ce and Au/HMS–Fe samples show smaller sharpness of their adsorption isotherms indicating poorer pore uniformity.

For all catalysts, the specific area (S_{BET}), cumulative pore volume (V_{total}) and pore diameter are compiled in Table 1. From this table, the S_{BET} and V_{total} values follow similar order (Au/HMS–Ti > Au/HMS > Au/HMS–Fe > Au/HMS–Ce). Both Au/HMS and Au/HMS–Ti samples show much broader pore size distribution (in the range 2–10 nm) than their Au/HMS–Fe and Au/HMS–Ce counterparts (in range 2–6 nm).

The total concentration of acid sites (expressed as mol_{NH3}/m^2) is shown in Table 1. From this table, the acidity of the catalysts follows the trend: Au/HMS > Au/HMS–Ti > Au/HMS–Fe > Au/HMS–Ce. Thus, the HMS material modification with Ti and Ce ions led to both a lower and a larger decrease in overall support acidity.

3.1.2. X-ray diffraction

The hexagonal arrangement of all synthesized supports was confirmed by the low-angle XRD patterns (not shown here). The unique peak at ca. 1.8° was due to the diffraction plane [100]. The absence of higher order reflections, viz. [110], [200] and [210], could be due to finite size effects of very fine particle morphology or due to the more disordered hexagonal framework structure of the samples [36]. For all supports, the d_{100}-spacing calculated from the X-ray patterns follows the trend: HMS–Ce (6.94 nm) > HMS (6.89 nm) > HMS–Ti (6.72 nm) > HMS–Fe (5.96 nm). Such a trend indicates that the HMS–Fe showed the largest incorporation of its guest ions within the framework structure of the HMS material, whereas ceria might form some separate clusters supported on the HMS but not embedded in its framework.

The wide-angle XRD patterns of the calcined catalysts are shown in Fig. 1. As seen in this figure, all calcined catalysts exhibit peaks positioned at 2θ values of 38.3° and 44.6°, which are attributed to [111] and [200] planes, respectively, of Au° crystals. Additionally, the Au/HMS–Ce shows the peaks positioned at 2θ values of 26.8° and 55.6°, which are indicative of the planes of CeO_x particles, respectively. On the other hand, from the peaks for Au/HMS–Fe, the evidence for the presence of Fe_2O_3 was deduced from a broad peak line at $2\theta = 23.0°$. Au/HMS–Ti catalyst does not show any evidence of TiO_2 crystallites.

3.1.3. UV–vis spectroscopy

To gain insight into the effect of HMS doping with Ce, Fe and Ti, the UV–vis diffuse reflectance spectra of the pure supports were recorded at room temperature in the range of 200–900 nm (Fig. 2). The electronic spectrum of Au/HMS–Ce shows a wide and intense absorption band in the region of 270–350 nm. Its interpretation is not easy due to the large band width and the specific reflectance, which is frequently observed in the Ce spectra. However, one could obtain information on surface coordination and oxidation states of Ce ions by measuring their *d–d* and *f–d* transitions and the oxygen–metal ion charge transfer bands [37]. The absorption band observed in the range of 270–350 nm could be associated with the electronic transition with charge transfer ($O^{2-} \rightarrow Ce^{4+}$) associated to Ce ions in SiO_2 [38], pointing again that ceria has not been incorporated in the framework but forms clusters on the surface of the HMS. On the other hand, the UV–vis spectrum of HMS–Fe shows a broad band of absorption at ca. 248 nm,

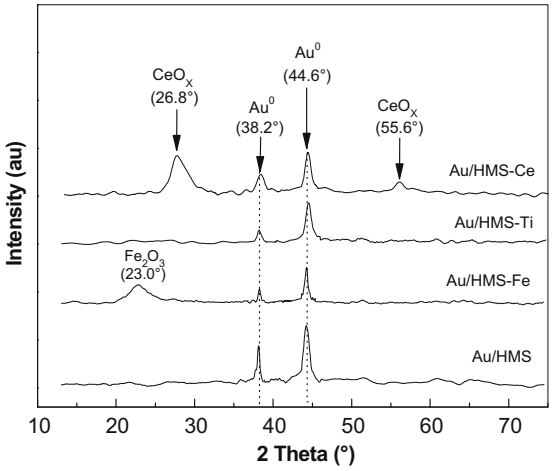

Fig. 1. XRD of the fresh Au/HMS–M (M = [–], Ce, Fe, Ti) catalysts.

Table 1
Some characteristics of the calcined catalysts and supports.

Samples	Au (wt.%)[a]	Ce_2O_3/ Fe_2O_3/TiO_2 (wt.%)[a]	S_{BET}[b] (m^2/g)	V_{total}[b] (cm^3/g)	d[b] (nm)	Acid sites[c] ($mmol_{NH3}/m^2$)
Au/HMS	2.24	–	521	1.1	8.2	0.70
Au/HMS–Ce	3.44	11.2	387	0.6	6.7	0.34
Au/HMS–Fe	2.84	5.8	460	0.8	7.0	0.46
Au/HMS–Ti	3.02	3.1	551	1.2	8.9	0.62

[a] As determined by chemical analysis (ICP technique) for the oxide precursors.
[b] Textural properties of the calcined catalysts as determined by N_2 adsorption–desorption isotherms: S_{BET}: specific surface area as calculated by BET equation; V_{total}: total pore volume; d: average pore diameter.
[c] Total amount of the acid sites of the pure supports.

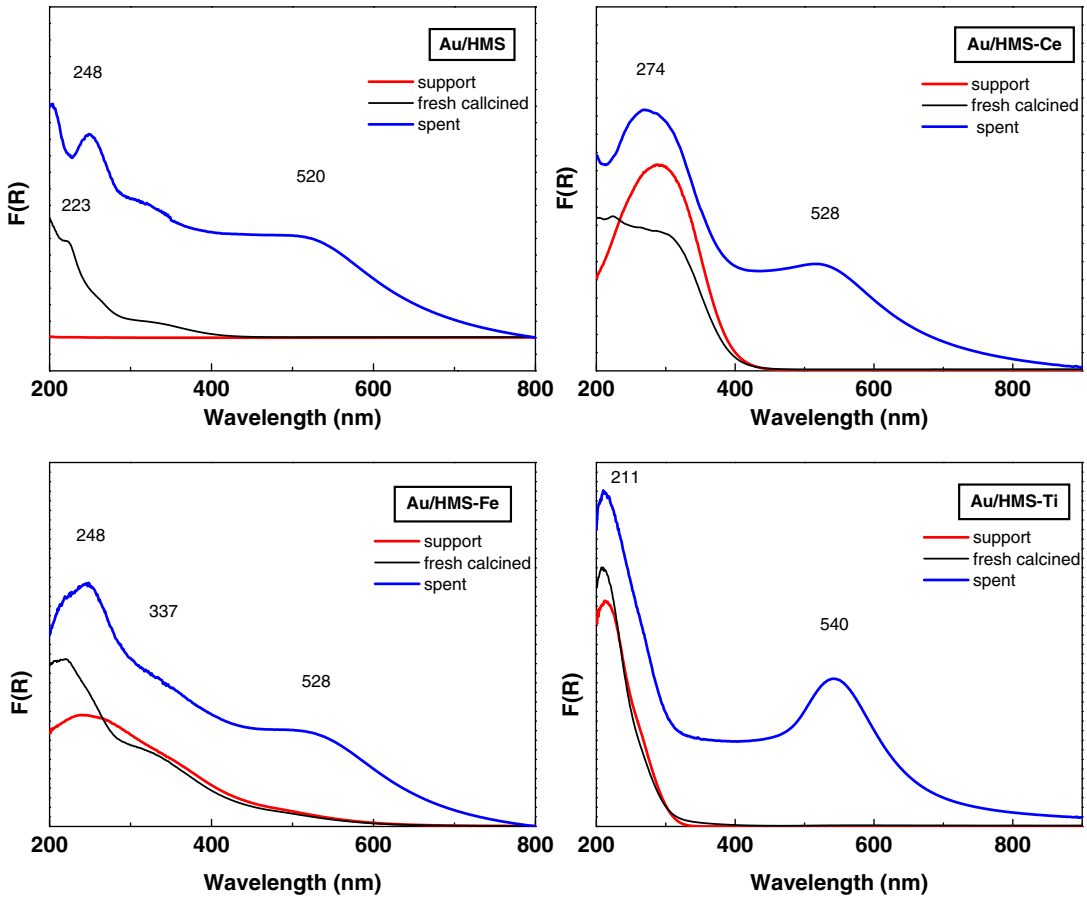

Fig. 2. UV-vis spectra of the support, fresh and spent Au/HMS–M (M = [–], Ce, Fe, Ti) catalysts.

confirming the incorporation into the HMS framework [39]. The observed shoulder at around 350 nm is characteristic of small FeO_x nanocrystallites [40]. The comparison of band intensities clearly indicates the major incorporation of Fe^{3+} ions into framework of HMS material. Finally, the HMS–Ti support shows one intense band at 211 nm which is usually assigned to isolated Ti^{4+} ions in a nearly tetrahedral coordination [41].

Fig. 2 also shows the UV–vis spectra of the calcined and spent catalysts (with Au). The absorption band at 248 nm observed in the spent Au/HMS and Au/HMS–Fe samples could be associated to the presence of charged gold species that are probably localized in the perimeter of the interface of Au particles with the support [42]. Contrary to the calcined catalysts, the UV–vis spectra of the spent Au catalysts show a band at ca. 530 nm which is usually assigned to plasmon or Au nanoparticles [43]. However, as this band is absent in the fresh catalysts, it can be reasonably assigned to coke residues [44]. Considering the higher adsorption of the deactivation catalyst (Fig. 2), it seems improbable that the leaching of Ce, Ti and Fe from the HMS is occurring during the reaction.

3.1.4. HRTEM measurements

The morphology of the surface of the reduced and the spent catalysts was studied by HRTEM technique. The size histograms of both forms of catalysts are compared in Fig. 3, the micrographs demonstrate that the Au nanoparticles have a rounded shape. Au/HMS–Ti catalyst shows ~70% of population of particles in the 1–2 nm range, ~60% of the particles of Au in the reduced Au/HMS and Au/HMS–Fe catalysts are in the 2–3 nm size range, while Au/HMS–Ce reduced catalyst shows the highest mean value and distribution of Au particle sizes (5.5 ± 1.8 nm).

Fig. 4 shows a micrograph of the Au/HMS–Ce catalyst where it can be observed that the ceria is not implanted in the framework of HMS but forming clusters on its surface in agreement with the UV–vis and XRD results. In the light of these results, two types of catalyst can be differentiated: on one hand, the Au supported on HMS, HMS–Ti and HMS–Fe, on the other hand the bimetallic Au–Ce supported on HMS since both metals form interacting domains on the surface of the support.

Fig. 4 also shows the intimate contact between CeO_2 and Au nanoparticles. However, around half of the population of Au particles remains isolated from CeO_2 particles. The CeO_2 particle size distribution has been determined for HMS–Ce support (prior to Au loading), indicating that most of the CeO_2 particles are around 4 nm but they have a broad distribution up to sizes larger than 10 nm. On top and although the procedure has been explained in the experimental section, differentiating Au from CeO_2 is not always straightforward; EDX analysis could prove the existence of Au and Ce in a single point but the contrast is not sufficient to determine the boundaries of the nanoparticles. As a result, we can conclude that the values of Au particle size for Au/HMS–Ce catalyst could be less accurate.

As compared with fresh reduced catalysts (Fig. 3), their spent counterparts showed a more heterogeneous distribution of Au^0 particles, with the Au/HMS–Fe catalyst being the one which shows the lowest increase of the Au^0 particle size during the reaction.

3.1.5. XPS measurements

The electronic properties of the support modifiers (Ti, Fe and Ce) and the Au were studied by XPS technique. The XP spectra of Au 4*f* core electron level of the fresh reduced and spent catalysts are shown in Figs. 5A and B. The binding energies values of the

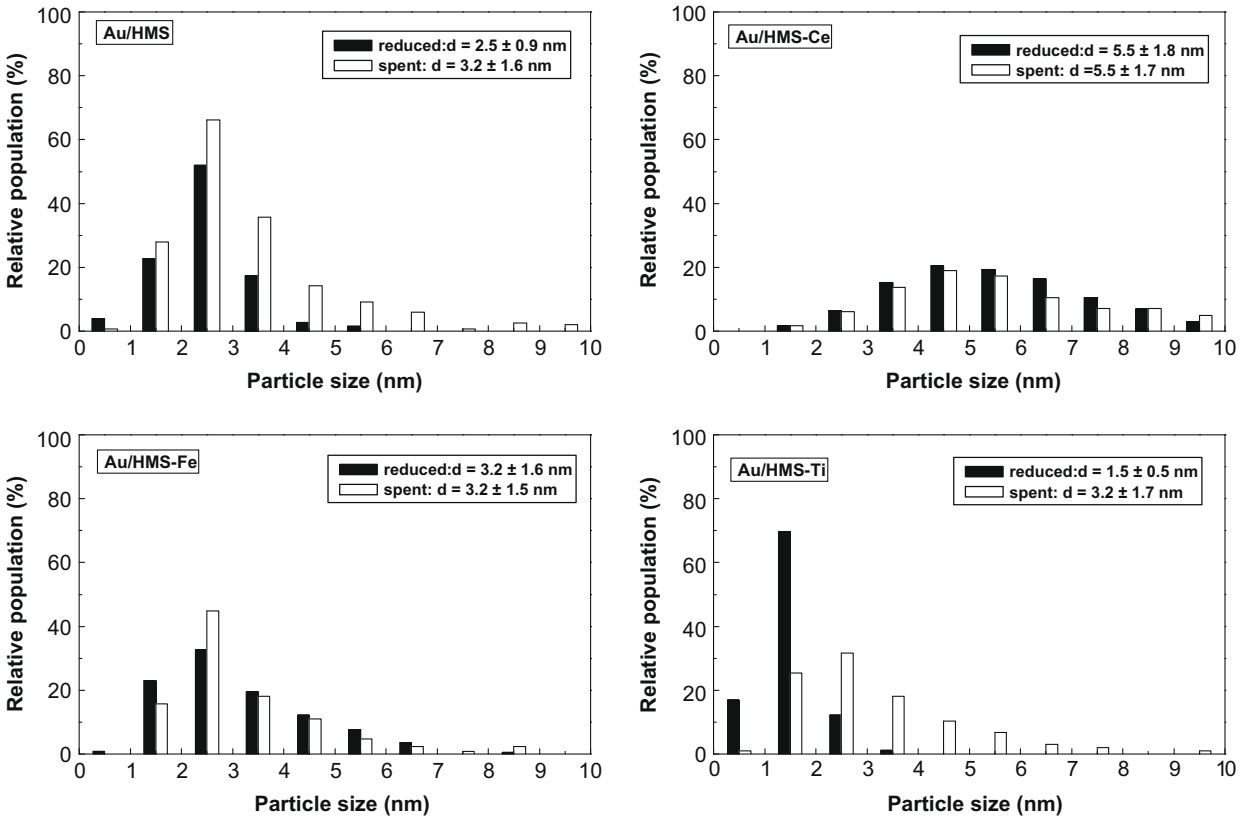

Fig. 3. Histograms of particle size distribution in the reduced and spent catalysts as obtained by HRTEM.

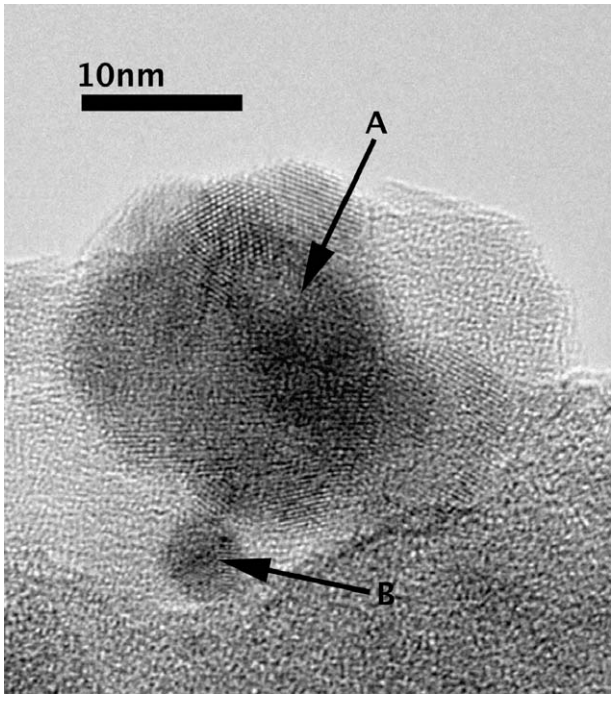

Fig. 4. Micrograph of a metallic cluster formed by Au (B) and CeO_2 (A) for the Au/HMS–Ce reduced catalyst.

most intense Au $4f_{7/2}$ peak are listed out in Table 2 along with the binding energies of the Ce $3d_{5/2}$, Fe $2p_{3/2}$ and Ti $2p_{3/2}$ core levels corresponding to Au/HMS–M (M = Ti, Fe, Ce), respectively. For all catalysts, the Au $4f_{7/2}$ binding energy (BE) was found at 83.7 eV (83.8 eV for Au/HMS–Fe, and this BE is typical of metallic Au [6]). After the reaction, the catalysts displayed an additional Au 4*f* doublet whose most intense Au $4f_{7/2}$ peak appeared at a BE of 85.3 eV, which can be assigned to very small positively charged metallic gold (assigned to $Au^{\delta+}$) interacting with support [45], see Table 2. Au/HMS–Ti and Au/HMS–Ce catalysts show much less presence of $Au^{\delta+}$ species by XPS, however, a direct evidence of AuO^-, AuO_2 and $AuOH^-$ ion clusters on supported Au catalysts has been recently reported by a time-of-flight secondary-ion mass-spectroscopy (TOF-SIMS), whereas the XPS of the same samples did not detect those species [17].

For the fresh reduced and spent Au/HMS–Ce catalysts (Fig. 6), the XP spectra of Ce 3*d* core electron level exhibited eight peaks corresponding to the spin-orbit doublet and satellite lines characteristic of oxidized state. The spin-orbit splitting is 18.4 eV. The Ce 3 $d_{5/2}$ and $3d_{3/2}$ showed the main features at 882.2, 884.6, 892.7 and 898.7 eV corresponding to *v*, *v*′,*v*″ and *v*‴, respectively, and the features at 902.2, 904.7, 907.4, and 916.9 correspond to *u*, *u*′,*u*″ and *u*‴ components, respectively [46]. Analyzing the features characteristic of each Ce^{4+} and Ce^{3+} species, it is evident that the proportion of the Ce^{4+} is three times higher than that of the Ce^{3+}.

The spectra of the fresh reduced and spent Au/HMS–Fe samples are compared in Fig. 6. For both fresh and used catalysts, the Fe $2p_{3/2}$ binding energy at 710.9 eV (or 710.6 eV for spent catalyst) and the signal shape indicated the presence of Fe^{3+} ions. The slight increase of the BE value (711.4 eV) of Fe $2p_{3/2}$ peak in the spent sample suggests the formation of some hydroxyl groups on the iron surface [47]. For both fresh reduced and spent forms of the Au/HMS–Ti catalyst (spectra not shown here), the component with BE of Ti $2p_{3/2}$ at 460.0 eV indicates unambiguously that Ti^{4+} ions are in a tetrahedral arrangement (Si–O–Ti), whereas the minor Ti $2p_{3/2}$ component at a BE of 458.5 eV is characteristic of titanium ions in an octahedral (Ti–O–Ti) coordination [48]. The proportion of these octahedral Ti–O–Ti species decreases after reaction sug-

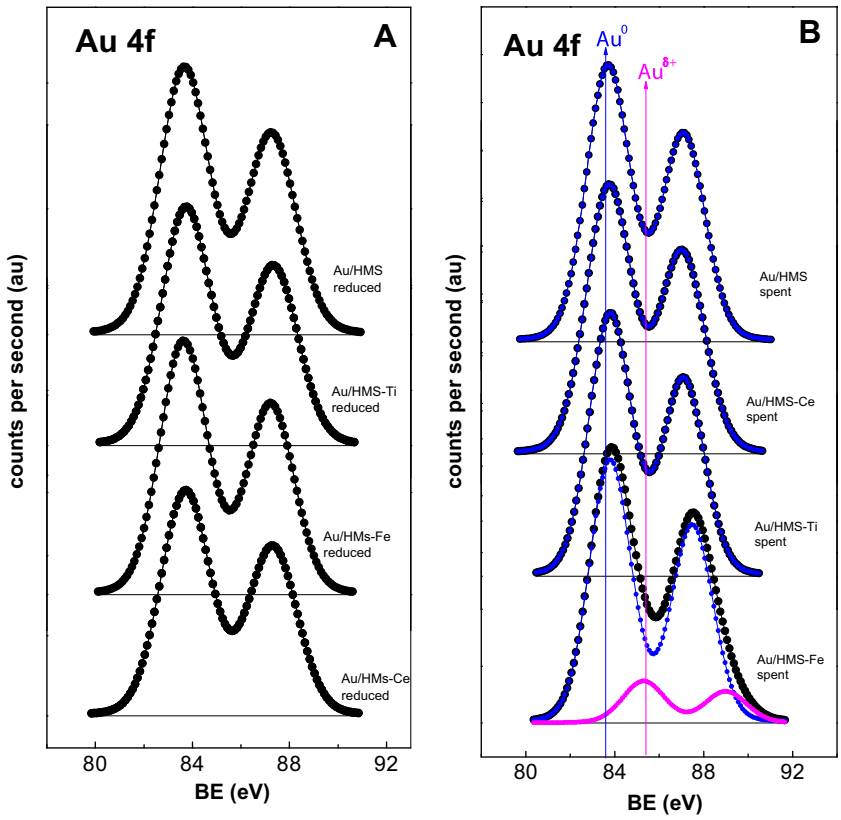

Fig. 5. XPS spectra of Au 4*f* core level for reduced (A) and spent (B) Au/HMS–M catalysts.

Table 2
Binding energies (eV) of core electrons and surface atomic ratios of the reduced (573 K, 1 h) and spent catalysts.

Catalyst	Si 2*p*	Au 4*f*	Ce 3*d* (Fe or Ti 2*p*)	Au/Si at ($Au^{\delta+}$/Si)	M/Si at (M = Ce, Fe, Ti)
Fresh reduced					
Au/HMS	103.4	83.7	–	0.0052	–
Au/HMS–Ce	103.4	83.7	882.5	0.0045	0.022
Au/HMS–Fe	103.4	83.8	710.9	0.0044	0.014
Au/HMS–Ti	103.4	83.7	458.5 (76) 460.0 (24)	0.0047	0.017
Spent					
Au/HMS	103.4	84.0 (89) 85.3 (11)	–	0.0061 (0.00067)	–
Au/HMS–Ce	103.4	83.9 (90) 85.2 (10)	882.0	0.0022 (0.00022)	0.010
Au/HMS–Fe	103.3	83.8 (82) 85.3 (18)	709.6 (43) 711.4 (57)	0.0041 (0.00078)	0.010
Au/HMS–Ti	103.4	83.9 (90) 85.2 (10)	458.6 (41) 459.9 (59)	0.0025 (0.00025)	0.022

gesting that some hydroxyl groups around the coordination sphere of Ti^{4+} are formed. Considering the information from UV–vis (Fig. 2) and HRTEM (Fig. 3) results, the smallest size of the Au^0 particles formed on Au/HMS–Ti catalyst could be linked with the large amount of TiO_2 species present on the support surface after reaction as detected by XPS.

From the Au/Si surface atomic ratios evaluated from XP spectra, it is clear that the cation M^{n+} incorporated into HMS–M has a strong influence on the distribution of the supported Au species (Table 2). Considering the Au/Si atomic ratio of the fresh reduced samples, the observed trend is: Au/HMS > Au/HMS–Ti ≈ Au/HMS–Ce > Au/HMS–Fe. Thus, Au exposure on all the cation-modified HMS–M substrates decreases with respect to the HMS one. This observation is in agreement with HRTEM analysis of the particle size and density.

3.2. Catalyst testing in biphenyl liquid-phase hydrogenation

The biphenyl liquid-phase hydrogenation was used to determine the activity of the supported Au catalysts. The kinetic behaviour of all catalysts was well modelled by the pseudo-first-order kinetics with respect to the batch space time (τ) from Eq. (3). Even though pseudo-first-order kinetic models have some limitations with respect to integral models [35], they are still useful for comparing the intrinsic activities close to differential conditions (conversion <20%). The kinetic performances of Au/HMS–M catalysts are displayed in Fig. 7 by means of the linear pseudo-first-order kinetic plot. Derived kinetic constants (in inverse units as τ) are summarized in the sub-graph of Fig. 7. In terms of the pseudo-first kinetic constant (k), Au/HMS–Fe catalyst displays the highest activity towards biphenyl hydrogenation. The value of the Weisz–Prater module of this experimental run (calculated using the rate in Fig. 7) was 0.045 assuring the minimal contribution of internal mass transfer limitations during the reaction.

It is expected that the acid sites could be involved in the hydrogenation mechanisms [49]. However, the direct contribution of the support to the hydrogenation rates is negligible based on (i) the low conversion (2.5%) obtained with the bare support (HMS) at the same conditions and (ii) the fact that the observed activity of the catalysts is not a function of their acidity (Table 1).

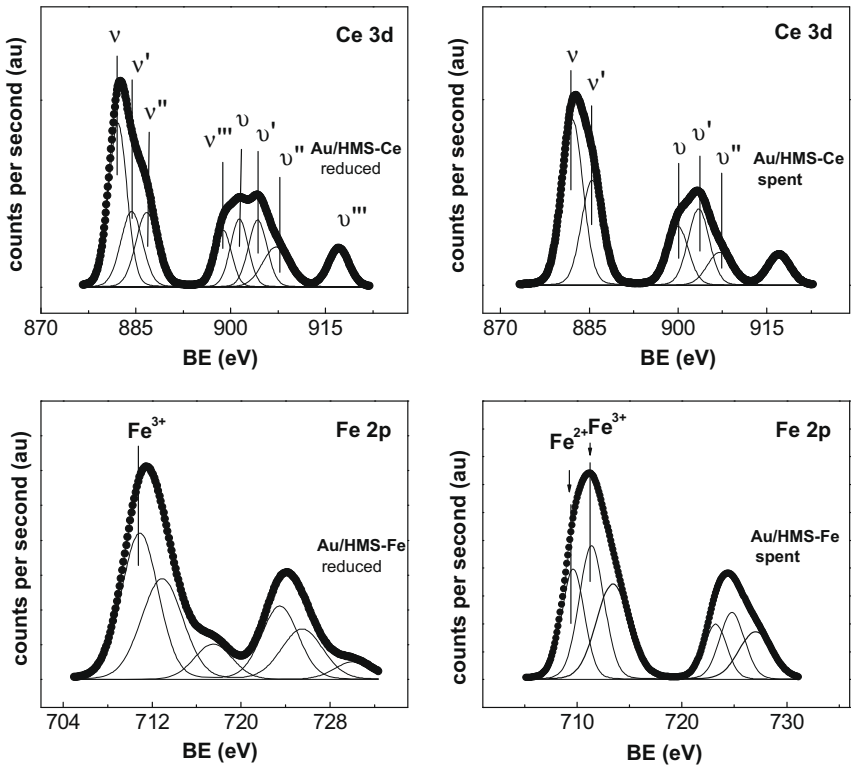

Fig. 6. XPS spectra of the Fe 2*p* and Ce 3*d* core electron levels for reduced Au/HMS–Fe and Au/HMS–Ce catalysts.

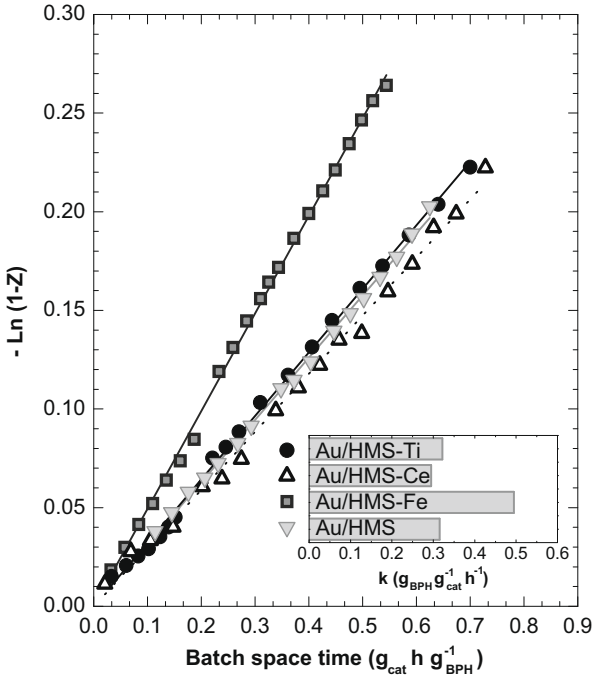

Fig. 7. Pseudo-first kinetic performance of the studied Au catalysts and their kinetic constants calculated from the slopes. Reaction conditions: 5 MPa, 488 K.

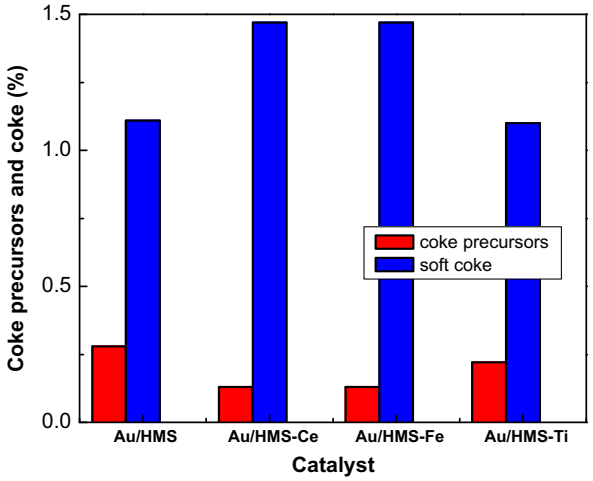

Fig. 8. Comparison of the type of coke formed on the different catalysts (TPO).

3.3. Characterization of the spent catalyst

The properties of the spent catalysts have been previously compared to those of the fresh catalysts by UV–vis spectroscopy (Fig. 2), HRTEM (Fig. 3) and XPS (Fig. 5) techniques. The comparison of the size distribution of Au particles (by processing HRTEM) of the fresh-spent catalysts (Fig. 3) allows us to conclude that there is certain sintering of the Au/HMS-Ce and Au/HMS–Ti catalysts, while the Au particle size distribution of Au/HMS and Au/HMS–Fe catalysts remains almost unaffected, in particular the Fe-containing catalyst.

The spent catalysts were characterized also by temperature-programmed oxidation (TPO) experiments. Fig. 8 shows the weight loss percentage of the samples corresponding to the temperature of combustion: 300–500 K, coke precursors and 500–800 K, "soft coke". The total amount of carbonaceous deposits in all the catalysts is similar; ~1.4% and the ratio of coke precursors to soft coke is also very similar indicating that neither the incorporation of metals into the HMS framework nor the Au properties affect the coke deposition.

4. Discussion

All the Au-supported catalysts (Au/HMS–M) proved to be active in the liquid-phase hydrogenation of biphenyl, the activity per gram of catalyst or metal is, however, substantially lower than that of Pt–Pd/Al_2O_3 catalyst upon similar reaction conditions [35]. This means that the implementation of Au-supported catalyst is not justified in terms of its activity, but could be justified in terms of stability.

The reaction rates expressed as TOF (in molecule of biphenyl converted per second and per exposed atom of Au, calculated using Eq. (4)) and QTOF (in molecule of biphenyl converted per second and per total atom of Au, calculated using Eq. (5)) are plotted in Fig. 9 vs. the exposure of $Au^{\delta+}$ species (measured by XPS, Table 2). As seen, Au/HMS–Fe catalyst shows the higher aromatic hydrogenation rate, the modification of the catalyst with Ti decreased the activity with respect to the Au/HMS catalyst. Besides, a linear correlation is observed for both TOF and QTOF with respect to the $Au^{\delta+}$ exposure, except for the Au/HMS–Ce catalyst which shows an higher TOF value than expected (in red, Fig. 9). This outlier comes from the particular state of the metallic phases in the Au/HMS–Ce catalyst, which form clusters of Au–CeO_2 onto the HMS support (Fig. 4), thus making the measurement of Dp_{Au} less accurate, which is required for calculating TOF in Eq. (4).

Bicyclohexyl (BCH) is the most interesting product due to its cetane number. Fig. 10 represents the selectivity of BCH versus BPH conversion (X) for all the catalysts, and the bare HMS support. Considering the fact that this is a reaction in series with two reaction rates (k_1 and k_2), Fig. 10 indicates that at the same BPH conversion level, k_2 is faster relative to k_1 for the Au/HMS–Fe catalyst (in the order: Au/HMS–Fe > Au/HMS–Ce > Au/HMS–Ti > Au/HMS). As a result, the doping of Fe in the Au/HMS catalyst enhances both hydrogenation rates (k_1 and k_2) and k_2 in particular, leading to higher activity and selectivity of the most interesting product (BCH).

The trend in activity cannot be correlated with the acidic properties (Table 1), the textural properties (Table 1) or more importantly with the Au particle morphology (Table 2, Figs. 3 and 4).

The most active catalyst in terms of hydrogenation rate per $g_{cat}(k)$, per $g_{Au\text{-}exposed}$(TOF) and $g_{Au\text{-}total}$ (QTOF) is Au/HMS–Fe. Moreover Au/HMS–Fe catalyst enhances the second aromatic hydrogenation (k_2) over the first one (k_1). Interestingly, the observed QTOF correlates linearly with the exposure of $Au^{\delta+}$ species. For Au/HMS–Ce catalyst, the Ce is not incorporated in the framework creating nano-sized clusters of Au and CeO_2. The resulting interaction makes the differentiation of Au from CeO_2 cumbersome in HRTEM (yielding not reliable Dp_{Au}values), furthermore this interaction is able to influence the electronic properties of Au without forming $Au^{\delta+}$ species (Fig. 5) enhancing the aromatic hydrogenation. The lower activity of Au/HMS–Ti catalyst can be explained taking into account the blockage of Au nanoparticles caused by titania coverage and/or Au sintering, as derived from the lower Au/Si atomic ratio of the spent catalyst with respect to the fresh counterpart (XPS results, Table 2).

5. Conclusions

Au nanoparticles supported on modified HMS with Ce, Fe and Ti were synthesized by deposition–precipitation method, characterized (fresh and spent) and tested in the liquid-phase biphenyl hydrogenation. The obtained results can be summarized as follows:

- The modification of HMS by Ce and Fe leads to Au-supported catalysts that are more stable in terms of sintering. The enhancement of biphenyl hydrogenation with respect to Au/HMS catalyst only occurs when Fe is incorporated into the framework of HMS.

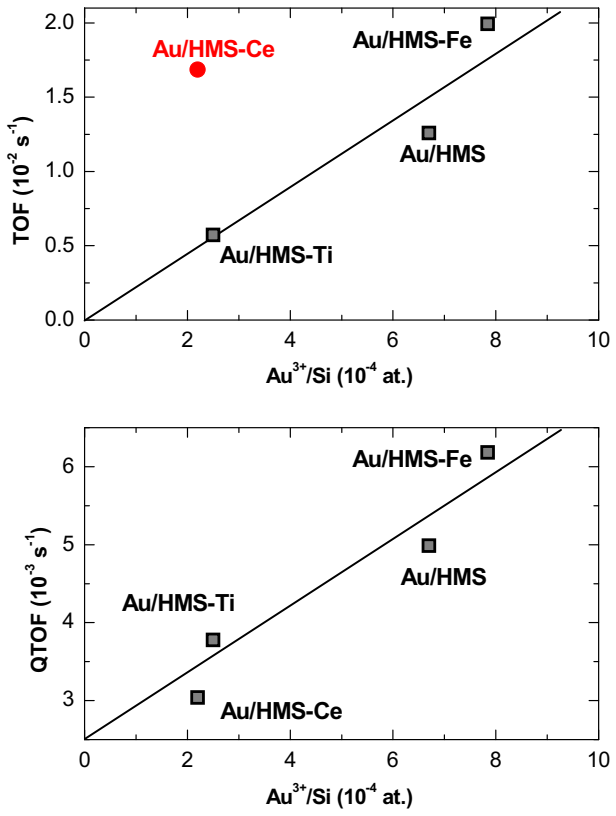

Fig. 9. (a) Linear correlation between TOF and the $Au^{\delta+}$/Si atomic ratio as measured by XPS (b) Linear correlation between QTOF and the $Au^{\delta+}$/Si atomic ratio as measured by XPS.

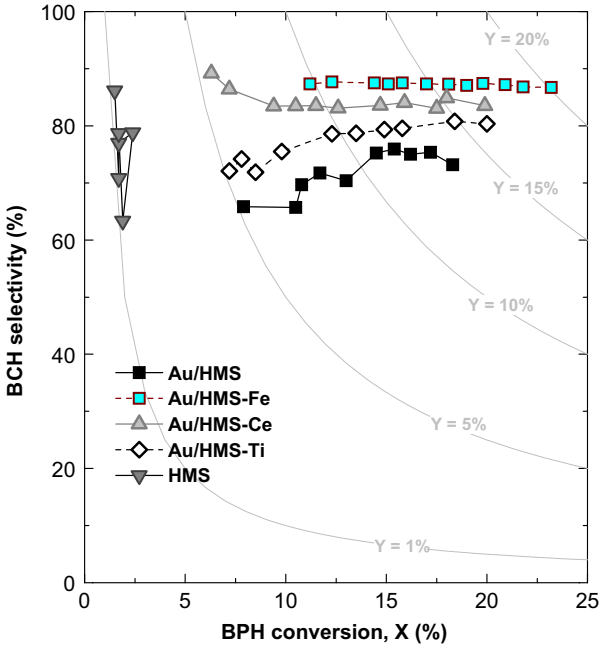

Fig. 10. Selectivity of bicyclohexyl (BCH) versus biphenyl (BPH) conversion of the catalyst used and the bare support. Reaction conditions at 488 K and 5 MPa. The grey lines represent the yields (Y) of BCH.

- The critical parameter when designing Au supported on HMS catalyst is the exposure of $Au^{\delta+}$ species. Indeed, a linear correlation between this parameter and the activity, in terms of QTOF, is presented.
- In the Au/HMS–Ce catalyst, Ce is not incorporated into the framework of HMS leading to clusters of Au and CeO_2. This causes the difficulty of calculating accurate values of Dp_{Au} from HRTEM.
- The modification of HMS by Ti does not lead to any enhancement of the hydrogenation performance of the Au/HMS catalyst due to the sintering of Ti (confirmed by XPS) which blocks part of the Au surface.
- The Au/HMS–Fe is the most promising catalyst for the hydrogenation of aromatics due to its enhanced stability and second aromatic-ring hydrogenation rate.

However, further investigation on the nature of the interaction Au–CeO_2 could yield more explanations with regard to the performance of Au/HMS–Ce catalyst. The intrinsic activity per g_{metal} (exposed, TOF; and total, QTOF) of all Au/HMS–M catalysts is substantially lower than that of Pt–Pd-supported catalyst so that new approaches are required for the application of Au-supported catalyst in hydroprocessing of aromatics.

Acknowledgments

Financial support by CSIC, Comunidad de Madrid (project CCG07-CSIC/ENE-1884) is gratefully acknowledged. T.A.Z. wishes to express his gratitude to the CNyN-UNAM (Mexico) for a postdoctoral bursary. The authors are grateful to G. Hosford, Dr. M. Peña and Dr. R. Guil-López for their help.

References

[1] S.K. Samanta, O.V. Singh, R.K. Jain, Trends Biotechnol. 20 (2002) 243.
[2] P.J. Tsai, T.S. Shih, H.L. Chen, W.J. Lee, C.H. Lai, S.H. Liou, Atmos. Environ. 38 (2004) 333.
[3] A. Stanislaus, B.H. Cooper, Catal. Rev.Sci. Eng. 36 (1994) 75.
[4] G.C. Bond, D.T. Thompson, Catal. Rev. Sci. Eng. 41 (1999) 319.
[5] M. Haruta, N. Yamada, T. Kobayashi, S. Iijima, J. Catal. 115 (1989) 301.
[6] M.P. Casaletto, A. Longo, A.M. Venezia, A. Martorana, A. Prestianni, Appl. Catal. A: Gen. 302 (2006) 309.
[7] A.S.K. Hashmi, G.J. Hutchings, Angew. Chem. Int. Ed. 45 (2006) 7896.
[8] P. Claus, Appl. Catal. A: Gen. 291 (2005) 222.
[9] A.M. Venezia, V. La Parola, B. Pawelec, J.L.G. Fierro, Appl. Catal. A: Gen. 264 (2004) 43.
[10] B. Pawelec, A.M. Venezia, V. La Parola, S. Thomas, J.L.G. Fierro, Appl. Catal. A: Gen. 283 (2005) 165.
[11] B. Pawelec, A.M. Venezia, V. La Parola, E. Cano-Serrano, J.M. Campos-Martin, J.L.G. Fierro, Appl. Surf. Sci. 242 (2005) 380.
[12] A.M. Venezia, V. La Parola, G. Deganello, B. Pawelec, J.L.G. Fierro, J. Catal. 215 (2003) 317.
[13] A.M. Venezia, V. La Parola, V. Nicoli, G. Deganello, J. Catal. 212 (2002) 56.
[14] A. Hugon, L. Delannoy, C. Louis, Gold Bull. 41 (2008) 127.
[15] X. Zhang, H. Shi, B. Xu, Angew. Chem. Int. Ed. 44 (2005) 7132.
[16] X. Zhang, H. Shi, B.-Q. Xu, Catal. Today 122 (2007) 330.
[17] L. Fu, N.Q. Wu, J.H. Yang, F. Qu, D.L. Johnson, M.C. Kung, H.H. Kung, V.P. Dravid, J. Phys.Chem. B 109 (2005) 3704.
[18] X. Zhang, F.X. Llabrés i Xamena, A. Corma, J. Catal. 265 (2009) 155.
[19] R. Nava, J. Morales, G. Alonso, C. Ornelas, B. Pawelec, J.L.G. Fierro, Appl. Catal. A: Gen. 321 (2007) 58.
[20] B. Pawelec, S. Damyanova, R. Mariscal, J.L.G. Fierro, I. Sobrados, J. Sanz, L. Petrov, J. Catal. 223 (2004) 86.
[21] T.A. Zepeda, B. Pawelec, J.L.G. Fierro, T. Halachev, J. Catal. 242 (2006) 254.
[22] T.A. Zepeda, B. Pawelec, J.L.G. Fierro, T. Halachev, Appl. Catal. B: Environ. 71 (2007) 223.
[23] T. Chiranjeevi, P. Kumar, S.K. Maity, M.S. Rana, G.M. Dhar, T. Rao, Micropor. Mesopor. Mater. 44 (2001) 547.
[24] N.Y. He, J.M. Cao, S.L. Bao, Q.H. Xu, Mater. Lett. 31 (1997) 133.
[25] H. Liu, G.Z. Lu, Y.L. Guo, Y. Guo, J.S. Wang, Micropor. Mesopor. Mater. 108 (2008) 56.
[26] K. Bachari, J.M.M. Millet, B. Benaichouba, O. Cherifi, F. Figueras, J. Catal. 221 (2004) 55.
[27] C. Milone, R. Ingoglia, L. Schipilliti, C. Crisafulli, G. Neri, S. Galvagno, J. Catal. 236 (2005) 80.
[28] S.C. Laha, P. Mukherjee, S.R. Sainkar, R. Kumar, J. Catal. 207 (2002) 213.
[29] B. Campo, M. Volpe, S. Ivanova, R. Touroude, J. Catal. 242 (2006) 162.
[30] P.T. Tanev, T.J. Pinnavaia, Science 267 (1995) 865.
[31] C.T. Kresge, M.E. Leonowicz, W.J. Roth, J.C. Vartuli, J.S. Beck, Nature 359 (1992) 710.
[32] M.R. Riazi, Y.A. Roomi, Chem. Eng. Sci. 62 (2007) 6649.
[33] M.R. Riazi, J.H. Vera, Ind. Eng. Chem. Res. 44 (2005) 186.
[34] S. Toppinen, T. Salmi, T.K. Rantakyla, J. Aittamaa, Ind. Eng. Chem. Res. 36 (1997) 2101.
[35] P. Castaño, D. van Herk, M.T. Kreutzer, J.A. Moulijn, M. Makkee, Appl. Catal. B: Environ. 88 (2009) 213.
[36] P.T. Tanev, M. Chibwe, T.J. Pinnavaia, Nature 368 (1994) 321.
[37] B.M. Weckhuysen, R.A. Schoonheydt, Catal. Today 49 (1999) 441.
[38] R.X. Li, S. Yabe, M. Yamashita, S. Momose, S. Yoshida, S. Yin, T. Sato, Mater. Chem. Phys. 75 (2002) 39.
[39] Y. Wang, Q.H. Zhang, T. Shishido, K. Takehira, J. Catal. 209 (2002) 186.
[40] K. Bachari, J.M.M. Millet, P. Bonville, O. Cherifi, F. Figueras, J. Catal. 249 (2007) 52.
[41] S. Perathoner, P. Lanzafame, R. Passalacqua, G. Centi, R. Schlogl, D.S. Su, Micropor. Mesopor. Mater. 90 (2006) 347.
[42] A.N. Pestryakov, V.V. Lunin, A.N. Kharlanov, N.E. Bogdanchikova, I.V. Tuzovskaya, Europ. Phys. J. D 24 (2003) 307.
[43] P. Claus, A. Bruckner, C. Mohr, H. Hofmeister, J. Am. Chem. Soc. 122 (2000) 11430.
[44] F. Bauer, H.G. Karge, Characterization of coke on zeolites, in: H.G. Karge, J. Weitkamp (Eds.), Molecular Sieves. Science and Technology, Characterization II, Vol. 5, Springer-Verlag, Berlin-Heidelberg, 2007, p. 282.
[45] D.A. Bulushev, I. Yuranov, E.I. Suvorova, P.A. Buffat, L. Kiwi-Minsker, J. Catal. 224 (2004) 8.
[46] Z.Q. Zou, M. Meng, L.H. Guo, Y.Q. Zha, J. Hazar. Mater. 163 (2009) 835.
[47] P. Reyes, H. Rojas, J.L.G. Fierro, Appl. Catal. A: Gen. 248 (2003) 59.
[48] M.C. Capel-Sanchez, J.M. Campos-Martin, J.L.G. Fierro, M.P. de Frutos, A.P. Polo, Chem. Commun. (2000) 855.
[49] J. Kanai, J.A. Martens, P.A. Jacobs, J. Catal. 133 (1992) 527.